

Nordmark map and the problem of large-amplitude chaos in impact oscillators

David J. W. Simpson 

School of Fundamental Sciences, Massey University, 4410, New Zealand

Viktor Avrutin 

Institute for Systems Theory and Automatic Control, University of Stuttgart, 70569, Germany

Soumitro Banerjee *

Department of Physical Sciences, Indian Institute of Science Education and Research, Kolkata 741246, India



(Received 20 March 2020; accepted 24 July 2020; published 21 August 2020)

Physical experiments have long revealed that impact oscillators commonly exhibit large-amplitude chaos over a narrow band of parameter values close to grazing bifurcations. This phenomenon is not explained by the square-root singularity of the Nordmark map, which captures the local dynamics to leading order, because this map does not exhibit such dynamics. In this paper, we compare a Poincaré map for a prototypical impact oscillator model with the corresponding Nordmark map. Though the maps agree to leading order, the Poincaré map exhibits a large-amplitude chaotic attractor while the Nordmark map does not because part of the attractor resides in a region of phase space where the two maps differ significantly.

DOI: [10.1103/PhysRevE.102.022211](https://doi.org/10.1103/PhysRevE.102.022211)

I. INTRODUCTION

An impact oscillator is most simply a periodically forced system that hits a barrier whenever its displacement reaches a threshold value [1,2]. Recurring impacts arise when the maximum displacement of regular oscillatory motion equals this value. This event is known as a *grazing bifurcation*.

It has long been known that chaotic dynamics is prevalent near grazing bifurcations [3,4]. A plausible explanation for this is the presence of a square-root singularity in return maps that captures the local dynamics. Such a map was first obtained by Nordmark [5] and can be written as

$$\begin{bmatrix} x \\ y \end{bmatrix} \mapsto \begin{cases} \begin{bmatrix} \tau & 1 \\ -\delta & 0 \end{bmatrix} \begin{bmatrix} x \\ y \end{bmatrix} + \begin{bmatrix} 0 \\ \mu \end{bmatrix}, & x \leq 0, \\ \begin{bmatrix} \tau & 1 \\ -\delta & 0 \end{bmatrix} \begin{bmatrix} x \\ y \end{bmatrix} + \begin{bmatrix} -\chi\sqrt{x} \\ \mu \end{bmatrix}, & x \geq 0. \end{cases} \quad (1)$$

We can think of (1) as an approximation to a Poincaré map between instances of zero velocity. The displacement x has been translated so that the threshold is $x = 0$. One iteration of (1) corresponds to an oscillation with no impact if $x < 0$, one impact if $x > 0$, and a zero-velocity impact (grazing) if $x = 0$. The parameters $\tau, \delta, \mu \in \mathbb{R}$ and $\chi = \pm 1$ are constants determined by the physical properties of the system.

As the impact velocity tends to zero (i.e., $x \rightarrow 0^+$), one entry in the Jacobian matrix of (1) tends to infinity in absolute value. This results in an infinite stretching of phase space, and it was understood that this phenomenon is responsible for the onset of chaos at grazing (for a formal proof of chaos, see [6,7]).

However, a typical bifurcation diagram of the Nordmark map [8] involving chaos is shown in Fig. 1(a); see also [9,10]. It may be noticed that although there is a direct transition from a stable fixed point to chaos, the spread of the chaotic attractor grows gradually from zero, at least in the parameter ranges considered in most earlier work. Experimental observations and numerical simulations of ODE models instead reveal chaos of relatively large amplitude over a small interval of parameter values near grazing [Fig. 1(b)]. This phenomenon [11,12], referred to as *narrow-band chaos* [13], is evidently not well captured by the Nordmark map.

Narrow-band chaos was studied for a prototypical model in [11]. Numerical investigations of a stroboscopic map revealed that a large-amplitude chaotic attractor is formed from the unstable manifold of a saddle-type period-3 orbit (an orbit involving three loops per period). It was further found that the size of the basin of attraction of the periodic orbit that undergoes grazing (a period-1 orbit) shrinks to zero at the grazing bifurcation. This is analogous to “dangerous” border-collision bifurcations for piecewise-smooth maps that do not involve a square-root singularity [14,15].

But the following question remains: Why does the Nordmark map fail to capture the narrow-band chaos? To address this question, we carefully construct a Poincaré map and explicitly perform coordinate changes so that it matches the Nordmark map (1) to leading order. In these coordinates, the large-amplitude chaotic attractor is seen to explore parts of phase space far from the point of grazing where the Poincaré map differs significantly from the Nordmark map. So the narrow-band chaos is a *global* phenomenon that occurs beyond the domain of validity of the *local* approximation provided by (1). For instance, the chaos involves high-velocity impacts while the Nordmark map is derived for impacts of low

*soumitro@iiserkol.ac.in

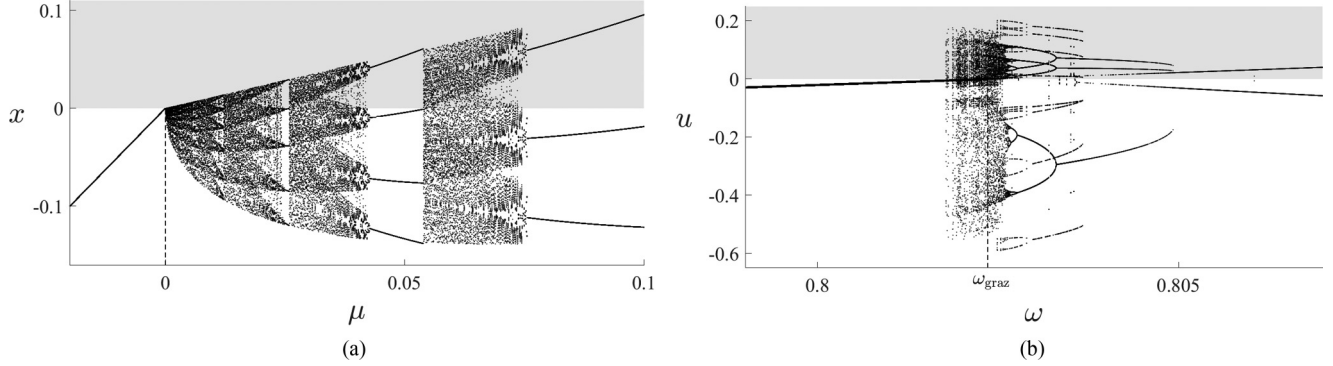


FIG. 1. (a) A typical bifurcation diagram of the Nordmark map (1) showing the appearance of a chaotic attractor at the grazing bifurcation (the parameter values are $\tau = 0.9$, $\delta = 0.1$, and $\chi = 1$). (b) A typical bifurcation diagram of the impact oscillator (2) showing a narrow-band of chaos [the parameter values are (3) and $\beta = 29$]. For both diagrams, each point in the upper (shaded) part corresponds to one oscillation with an impact, while each point in the lower (unshaded) part corresponds to one oscillation without an impact.

velocity. The Nordmark map, however, correctly predicts the absence of a local attractor immediately beyond the grazing bifurcation.

The remainder of this paper is organized as follows. We state the model equations for an oscillator with soft impacts in Sec. II and calculate the grazing bifurcation in Sec. III. We then briefly investigate a Poincaré map for this model and find that the grazing bifurcation does not involve a square-root singularity (Sec. IV). For this reason, we consider the hard impact limit in Sec. V (which does not seem to significantly affect the narrow-band chaos). A Poincaré map for the hard (or instantaneous) impact system involves a square-root singularity and is constructed in Sec. VI. We then compare the Poincaré and Nordmark maps in Sec. VII. We present some hitherto unexplored characters of the Nordmark map in Sec. VIII, including the occurrence of coexisting stable solutions that become important at grazing. Finally, we provide concluding remarks in Sec. IX.

II. THE IMPACT OSCILLATOR MODEL

We start our investigation with the typical “soft-impact” oscillator shown in Fig. 2 on which experimental and numerical investigations have been carried out in several previous works [11,12,16]. This system is modeled by the nondimensionalized equations

$$\begin{aligned} \dot{u} &= v, \\ \dot{v} &= -(u + e) - 2\xi v - \beta u H(u) + a\omega^2 \sin(\omega t). \end{aligned} \quad (2)$$

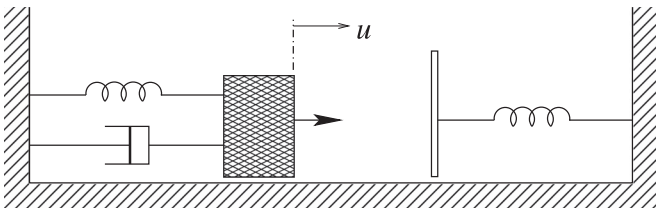


FIG. 2. A soft-impact oscillator modeled by (2), where $u = 0$ at grazing.

Here $u(t)$ and $v(t)$ represent the displacement and velocity of the oscillator that has damping ratio $\xi > 0$ and equilibrium at $u = -e < 0$. The forcing is harmonic with frequency $\omega > 0$ and scaled amplitude $a > 0$. The oscillator is assumed to impact and detach from an elastic beam at $u = 0$ so that while $u > 0$, the beam imparts a force of $-\beta u$, where $\beta > 0$; in (2) H is the Heaviside function.

Below we use ω as the primary bifurcation parameter, as this was a simple parameter to control in experiments [16]. Typical values of β corresponding to experiments are relatively large, in which case, as detailed in Sec. V, it is reasonable to treat the impacts as instantaneous. Figure 1(b) shows a bifurcation diagram of the soft-impact system with $\beta = 29$ and

$$\begin{aligned} a &= 0.7, \\ e &= 1.26, \\ \xi &= 0.02, \end{aligned} \quad (3)$$

which are based on values used in [12]. This figure shows large-amplitude chaos over a narrow band of ω -values close to the grazing bifurcation, $\omega = \omega_{\text{graz}}$. Next we calculate the value of ω_{graz} analytically.

III. A CALCULATION OF THE GRAZING BIFURCATION

If the forcing amplitude of (2) is sufficiently small, the system has a stable periodic orbit that does not involve impacts (i.e., its maximum value of u is negative). A grazing bifurcation occurs when its maximum value of u equals 0. Here we state the flow of the $u < 0$ part of (2) (which is available in closed form because with $u < 0$ the system is a harmonically forced linear oscillator). We then use this to obtain a formula for the value of ω at which the grazing bifurcation occurs. Similar calculations are performed in [17,18].

We can write (2) as

$$\begin{bmatrix} \dot{u} \\ \dot{v} \end{bmatrix} = \begin{cases} f_0(u, v, t), & u \leq 0, \\ f_\beta(u, v, t), & u \geq 0, \end{cases} \quad (4)$$

where

$$f_s(u, v, t) = \begin{bmatrix} 0 \\ -e \end{bmatrix} + A_s \begin{bmatrix} u \\ v \end{bmatrix} + \begin{bmatrix} 0 \\ a\omega^2 \sin(\omega t) \end{bmatrix} \quad (5)$$

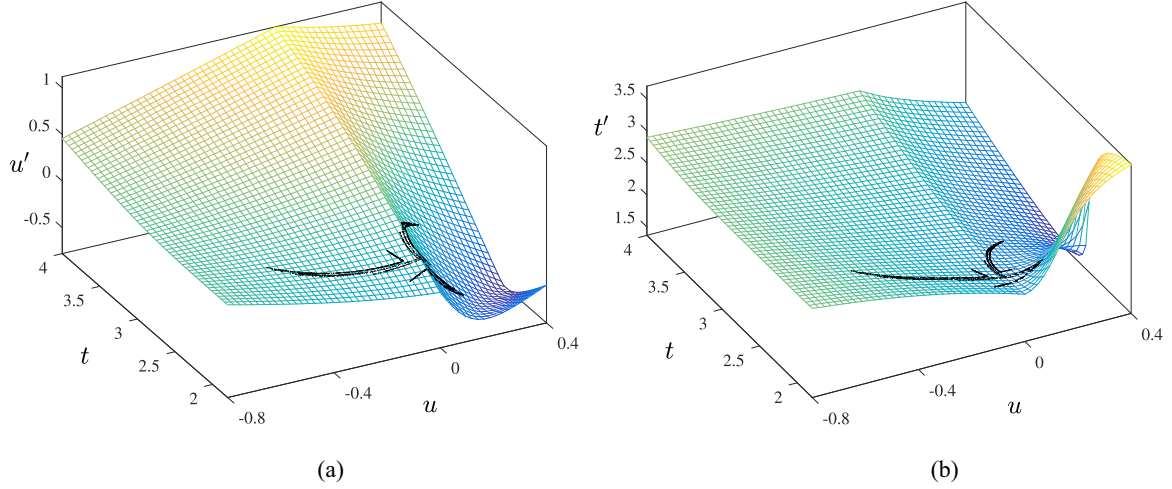


FIG. 3. Numerically obtained plots of the Poincaré map of the soft impacting system (3) at $\omega = \omega_{\text{graz}}$ using the parameters (3) and $\beta = 29$. The left figure shows the u -component of the map; the right figure shows the t -component. Given a point (u, t) on the Poincaré section $v = 0$, the point (u', t') is the next intersection of the corresponding forward orbit with $v = 0$ (and $\dot{v} < 0$; also points with $u > 0$ are virtual; see [18] or Sec. VI for the case of instantaneous impacts).

and

$$A_s = \begin{bmatrix} 0 & 1 \\ -(1+s) & -2\xi \end{bmatrix}. \quad (6)$$

The flow of $(\dot{u}, \dot{v}) = f_s(u, v, t)$ is

$$\Phi_s(t; u_0, v_0; t_0) = \Phi_s^{\text{part}}(t) + \Phi_s^{\text{homog}}(t; u_0, v_0; t_0), \quad (7)$$

with the particular solution

$$\begin{aligned} \Phi_s^{\text{part}}(t) &= \begin{bmatrix} \frac{-e}{1+s} \\ 0 \end{bmatrix} + \frac{a\omega^2}{(1+s-\omega^2)^2 + 4\xi^2\omega^2} \\ &\times \begin{bmatrix} -2\xi\omega & 1+s-\omega^2 \\ \omega(1+s-\omega^2) & 2\xi\omega^2 \end{bmatrix} \begin{bmatrix} \cos(\omega t) \\ \sin(\omega t) \end{bmatrix}, \end{aligned} \quad (8)$$

and the homogeneous solution

$$\Phi_s^{\text{homog}}(t; u_0, v_0; t_0) = e^{(t-t_0)A_s} \begin{pmatrix} u_0 \\ v_0 \end{pmatrix} - \Phi_s^{\text{part}}(t_0). \quad (9)$$

The stable periodic orbit is $\Phi_0^{\text{part}}(t)$ and attains its maximum value of u when $v = 0$. By solving $\Phi_0^{\text{part}}(t) = (0, 0)$ simultaneously for ω and t we obtain the values ω_{graz} and t_{graz} given implicitly by

$$\begin{aligned} (1-\omega^2)^2 + 4\xi^2\omega^2 &= \frac{a^2\omega^4}{e^2}, \\ \tan(\omega t) &= -\frac{1-\omega^2}{2\xi\omega}. \end{aligned}$$

With the parameter values (3) of Fig. 1(b), we have

$$\omega_{\text{graz}} = 0.802\,361\,97, \quad (10)$$

$$t_{\text{graz}} = 2.069\,704\,60, \quad (11)$$

to eight decimal places.

IV. THE CHARACTER OF A POINCARÉ MAP FOR SOFT IMPACTS

Figure 3 shows a Poincaré map of the soft impact oscillator at the grazing bifurcation (i.e., $\omega = \omega_{\text{graz}}$). This map was numerically constructed by using $v = 0$ as the Poincaré section. We omit a precise definition of this map (see, for instance, [18]) as below we focus our analysis on the case of instantaneous impacts. Indeed, different Poincaré sections yield topologically conjugate maps [19].

One iteration of the Poincaré map corresponds to one oscillation of (2). For $u < 0$, the oscillation involves no impact; for $u > 0$, the oscillation involves one impact. Consequently, the map is piecewise-smooth with *switching manifold* $u = 0$. In Fig. 3 we have plotted the map on a scale appropriate for the large-amplitude attractor (which is also shown) and to match later figures.

From a cursory inspection of Fig. 3 it appears that the Poincaré map has a square-root singularity in the form of a \sqrt{u} term for $u > 0$. However, (4) is continuous at the grazing point $(u, v) = (0, 0)$, hence the grazing bifurcation is an example of a *continuous grazing bifurcation* [9]. Consequently the Poincaré map is in fact differentiable on $u = 0$ and has a $\frac{3}{2}$ -type “singularity” [20]. This is not apparent in Fig. 3 because the scale is relatively large.

V. DYNAMICS WITH INSTANTANEOUS IMPACTS

The Poincaré map of Fig. 3 has a strong square-root character because the value $\beta = 29$ (chosen to match experiments) is relatively large. This parameter represents the effective spring constant of the elastic beam. In the limit $\beta \rightarrow \infty$ the time that the oscillator is in contact with the beam tends to zero, and the model (2) becomes

$$\begin{aligned} (\dot{u}, \dot{v}) &= f_0(u, v, t) && \text{while } u < 0, \\ (u, v) &\mapsto (u, -v) && \text{whenever } u = 0. \end{aligned} \quad (12)$$

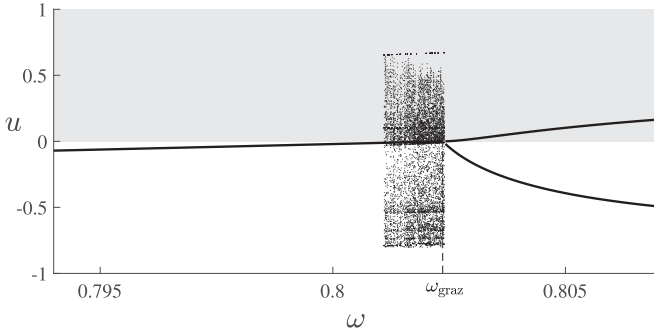


FIG. 4. A bifurcation diagram of the impact oscillator with instantaneous impacts (12) for the parameter values (3). This corresponds to (2) in the limit $\beta \rightarrow \infty$ [in contrast to Fig. 1(b), which uses $\beta = 29$]. Specifically this figure shows orbits of the Poincaré map P (13) with transient dynamics removed [Fig. 1(b) was computed in a similar fashion].

In this model, impacts are instantaneous with velocity reversal and no energy loss (i.e., the restitution coefficient is 1). For this system the grazing bifurcation occurs at the same value $\omega = \omega_{\text{graz}}$ but is now an *impacting grazing bifurcation* for which the analogous Poincaré map has a square-root singularity in the form of a \sqrt{u} -term for $u > 0$.

Figure 4 shows a bifurcation diagram of (12), and from this we see that the narrow-band chaos is retained in the hard impact limit. Figure 5 shows the Poincaré map and chaotic attractor at the grazing bifurcation. Although the size of the attractor has increased somewhat, on the scale shown the qualitative features of the map are essentially unchanged. For this reason, an analysis of the Poincaré map for instantaneous impacts is expected to be insightful for understanding the chaotic attractor of the system with soft impacts. Certainly the subject of our investigation is the square-root character of the map, and so we proceed by analyzing the model with instantaneous impacts.

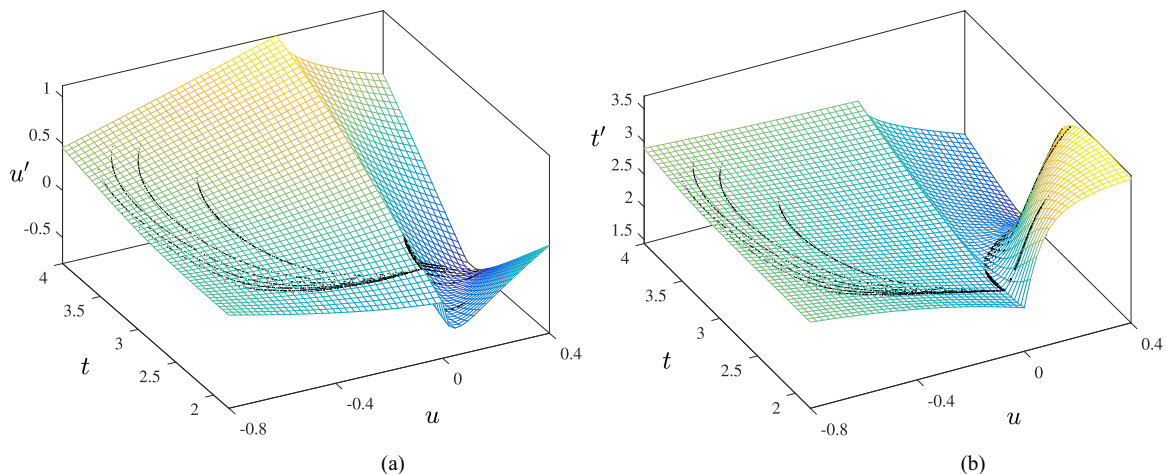


FIG. 5. Numerically obtained plots of the Poincaré map P of the system with instantaneous impacts (12) at the grazing bifurcation $\omega = \omega_{\text{graz}}$ using parameters (3). This figure corresponds to the limit $\beta \rightarrow \infty$ (Fig. 3 uses $\beta = 29$). Given a point (u, t) on the Poincaré section $v = 0$, the point $(u', t') = P(x, t)$ is defined by (13); see Fig. 6.

VI. CONSTRUCTION OF THE POINCARÉ MAP FOR INSTANTANEOUS IMPACTS

Here we construct the Poincaré map, let us call it P , for (12) using the method of Nordmark [5], which is now quite standard. For simplicity, we use $v = 0$ as the Poincaré section and write the map as $(u', t') = P(u, t)$, where t' is taken modulo $\frac{2\pi}{\omega}$. Whenever an impact occurs, the orbit jumps over $v = 0$; see Fig. 6. For this reason, we evolve the preimpact point (on the positive v -axis) forward via f_0 to obtain a point on $v = 0$ (with $u > 0$). This point is *virtual* in the sense that it does not represent an achievable state of the impacting system.

We express P as

$$P = P_{\text{smooth}} \circ P_{\text{disc}}, \quad (13)$$

where P_{smooth} is a *smooth map* corresponding to one excursion from $v = 0$ back to $v = 0$ as governed by the left-half system f_0 , and P_{disc} is the *discontinuity map* that provides the necessary correction to account for an impact. If $u \leq 0$, no correction is needed, so P_{disc} is the identity map. If $u > 0$, then, as illustrated in Fig. 6, P_{disc} maps the forward extension to $v = 0$ of a preimpact point to the backward extension to $v = 0$ of a postimpact point (where extension refers to evolution under f_0). Via lengthy calculations based on matching terms of a Taylor expansion of the flow $\Phi_0(t)$ [given by (7) with $s = 0$], we obtain for $u > 0$

$$P_{\text{disc}}(u, t; \omega) = \begin{bmatrix} u + \tilde{O}(3) \\ t - c\sqrt{u} + \tilde{O}(2) \end{bmatrix}, \quad (14)$$

where

$$c = \frac{2^{\frac{3}{2}}}{\omega_{\text{graz}}\sqrt{e}}, \quad (15)$$

and $\tilde{O}(k)$ denotes terms that are order k in \sqrt{u} , $t - t_{\text{graz}}$, and $\omega - \omega_{\text{graz}}$. Such calculations are detailed in [9,21].

Next we calculate the leading-order contribution of P_{smooth} in terms of the parameters of (12). First observe that at the grazing bifurcation ($\omega = \omega_{\text{graz}}$) the periodic orbit $\Phi_0^{\text{part}}(t)$ intersects $v = 0$ at $(u, t) = (0, t_{\text{graz}})$. Therefore,

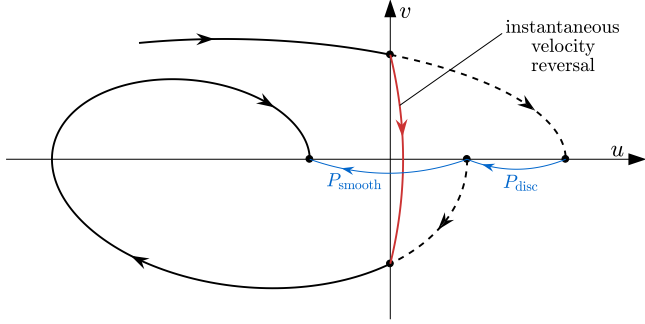


FIG. 6. An illustration of the Poincaré map P as the composition (13). The t -axis is omitted for simplicity.

$P_{\text{smooth}}(0, t_{\text{graz}}; \omega_{\text{graz}}) = (0, t_{\text{graz}})$. To first order the Taylor expansion of P_{smooth} about $(u, t; \omega) = (0, t_{\text{graz}}; \omega_{\text{graz}})$ can be written as

$$P_{\text{smooth}}(u, t; \omega) = \begin{bmatrix} 0 \\ t_{\text{graz}} \end{bmatrix} + J \begin{bmatrix} u \\ t - t_{\text{graz}} \end{bmatrix} + K(\omega - \omega_{\text{graz}}) + O(2), \quad (16)$$

where J is a 2×2 matrix and $K \in \mathbb{R}^2$. From the expressions (7)–(9) for the flow $\Phi_0(t)$ with $\omega = \omega_{\text{graz}}$, we obtain

$$J = Q^{-1} e^{\frac{2\pi}{\omega_{\text{graz}}} A_0} Q, \quad (17)$$

where

$$Q = \begin{bmatrix} \frac{1}{e\omega_{\text{graz}}} & 0 \\ 0 & \omega_{\text{graz}} \end{bmatrix}. \quad (18)$$

Also by differentiating $\Phi_0(t)$ with respect to ω , we obtain (after much simplification)

$$K = \frac{2}{a^2 \omega_{\text{graz}}^4} Q^{-1} \left(I - e^{\frac{2\pi}{\omega_{\text{graz}}} A_0} \right) \times \begin{bmatrix} a^2 \omega_{\text{graz}}^2 + e^2 (1 - \omega_{\text{graz}}^2 - 2\xi^2) \\ \xi e^2 (1 + \omega_{\text{graz}}^2) - \frac{a^2 \omega_{\text{graz}}^4 t_{\text{graz}}}{2} \end{bmatrix}. \quad (19)$$

We note that the analogous linear approximation to P_{smooth} given in [18] has a significantly simpler dependency on the parameters of the system. This is because the nondimensionalization used in [18] caused the values of e and ω to be scaled to 1 (at the cost of a nonunit spring constant and scaling time) so the matrix Q was not needed. Also here we have used the forcing frequency as the primary bifurcation parameter to align with the physical experiments. By instead using the forcing amplitude as the primary bifurcation parameter, K admits a simpler expression because it is easier to differentiate (8) with respect to a than with respect to ω .

Finally from (14) and (16) the composition (13) is given by

$$P(u, t; \omega) = \begin{bmatrix} 0 \\ t_{\text{graz}} \end{bmatrix} + \begin{cases} J \begin{bmatrix} u \\ t - t_{\text{graz}} \end{bmatrix} + K(\omega - \omega_{\text{graz}}), & u \leq 0, \\ J \begin{bmatrix} u \\ t - t_{\text{graz}} - c\sqrt{u} \end{bmatrix} + K(\omega - \omega_{\text{graz}}), & u \geq 0, \end{cases} + \text{h.o.t.}, \quad (20)$$

where h.o.t. denotes higher-order terms.

VII. A COMPARISON OF THE POINCARÉ MAP WITH THE NORDMARK MAP

To convert the Poincaré map P into the form of the Nordmark map (1), we omit the higher-order terms in (20) and apply the affine coordinate change,

$$\begin{bmatrix} x \\ y \\ \mu \end{bmatrix} = \frac{1}{J_{12}^2 c^2} \begin{bmatrix} 1 & 0 & 0 \\ -J_{22} & J_{12} & K_1 \\ 0 & 0 & (1 - J_{22})K_1 + J_{12}K_2 \end{bmatrix} \times \begin{bmatrix} u \\ t - t_{\text{graz}} \\ \omega - \omega_{\text{graz}} \end{bmatrix}, \quad (21)$$

where J_{ij} and K_i denote the elements of J and K .

The Poincaré map then becomes (1) with

$$\tau = \text{trace}(J), \quad \delta = \det(J), \quad \chi = \text{sgn}(J_{12}c). \quad (22)$$

For instance, with the parameter values (3) we have

$$\tau = 0.0422, \quad \delta = 0.7311, \quad \chi = 1, \quad (23)$$

to four decimal places.

Figure 7 shows a bifurcation diagram of the Nordmark map with these values. The stable fixed point with $x < 0$ that exists for $\mu < 0$ represents the stable nonimpacting periodic orbit, and $\mu = 0$ represents the grazing bifurcation. At the grazing bifurcation many unstable periodic solutions are created (see [10] for calculations of periodic solutions), but there is no

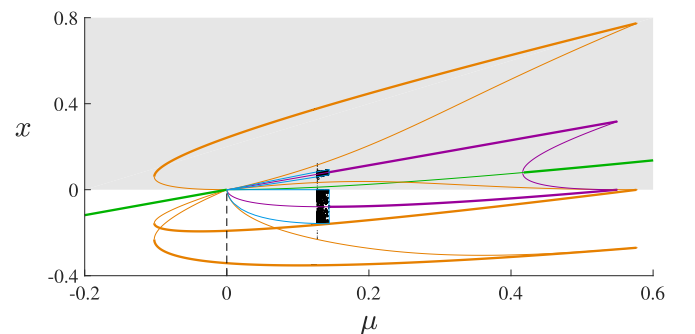


FIG. 7. A bifurcation diagram of the Nordmark map (1) with parameter values (23) (to four decimal places). Stable solutions are shown with thick curves; unstable solutions are shown with thin curves. Curves in the shaded part correspond to oscillations with an impact.

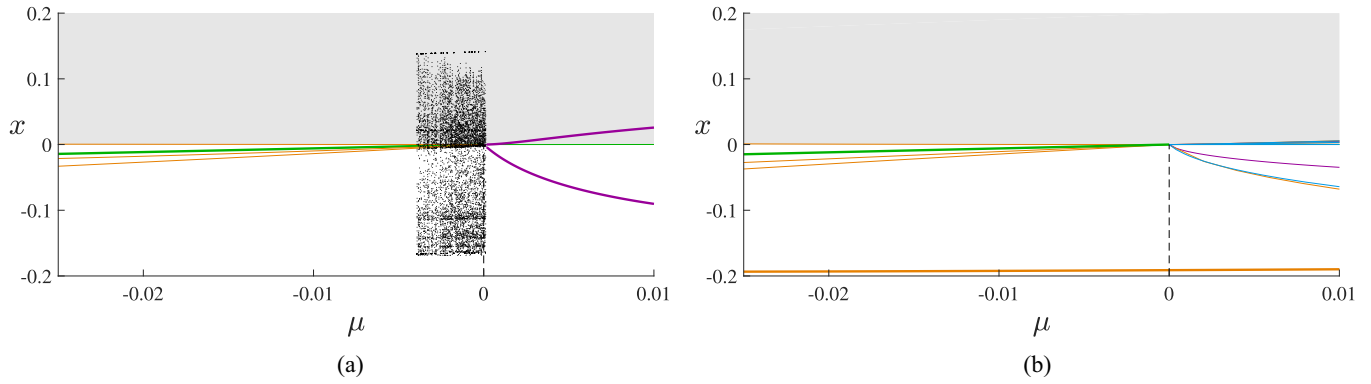


FIG. 8. (a) A bifurcation diagram of (12) (using the same parameter values as Fig. 4) in the coordinates of the Nordmark map. (b) A magnification of Fig. 7.

chaotic attractor at the grazing bifurcation. Instead there exists a stable period-3 solution.

The stable period-3 solution is created at a smooth saddle-node bifurcation at around $\mu \approx -0.1$ and disappears at a nonsmooth saddle-node bifurcation at $\mu \approx 0.58$. The unstable branches created at these bifurcations converge on the period-1 solution at the grazing parameter value, thus creating

a situation akin to a dangerous border collision bifurcation [15,22] where the basin of attraction of the main attractor reduces to zero size. Beyond the grazing bifurcation, orbits converge to the stable period-3 solution.

A chaotic attractor appears to exist for approximately $0.126 < \mu < 0.143$. We now show that this interval is significantly far beyond the grazing bifurcation and thus is almost

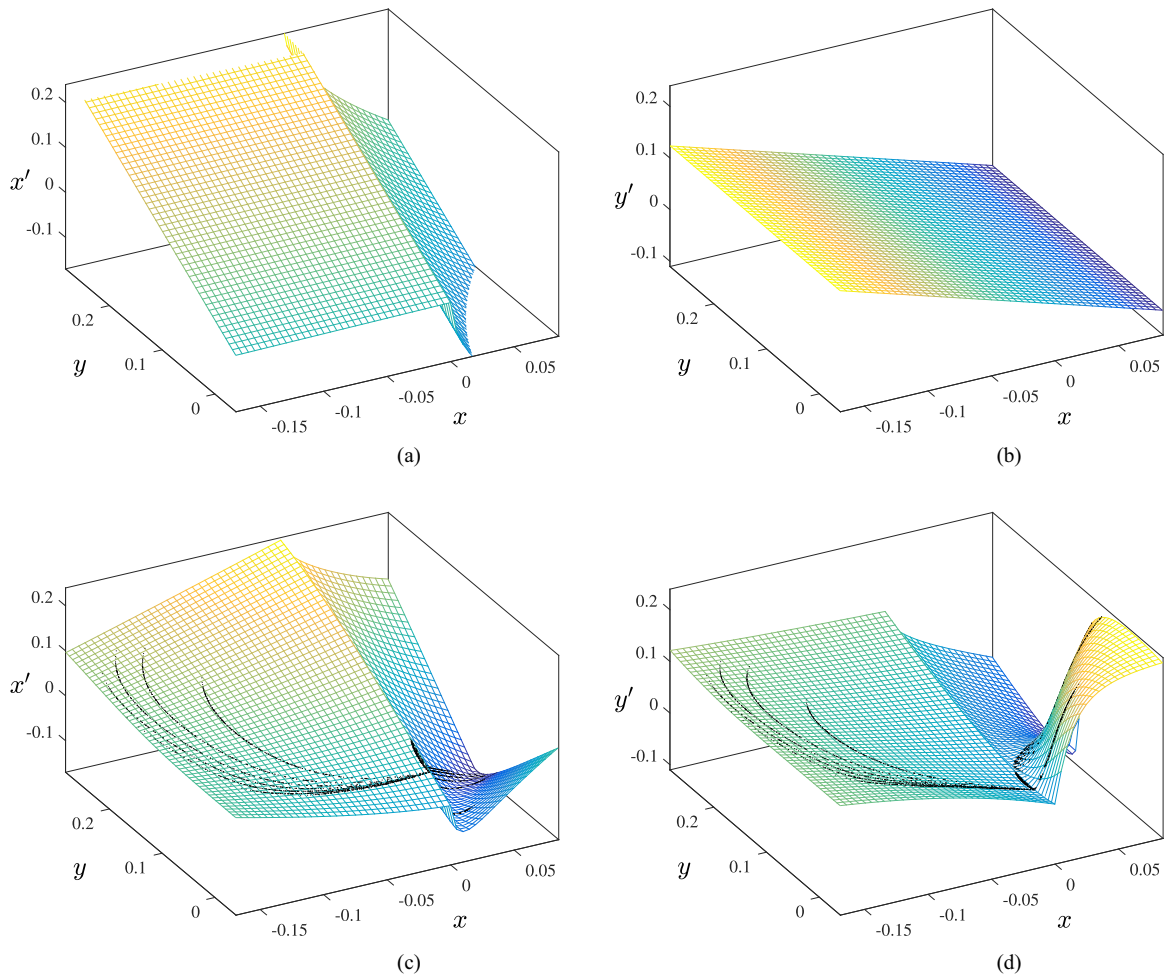


FIG. 9. Panels (a) and (b) show the Nordmark map (1) with (23) (to four decimal places) and $\mu = 0$. Panels (c) and (d) show the Poincaré map P in the coordinates (21) with parameters (3) and $\omega = \omega_{\text{graz}}$.

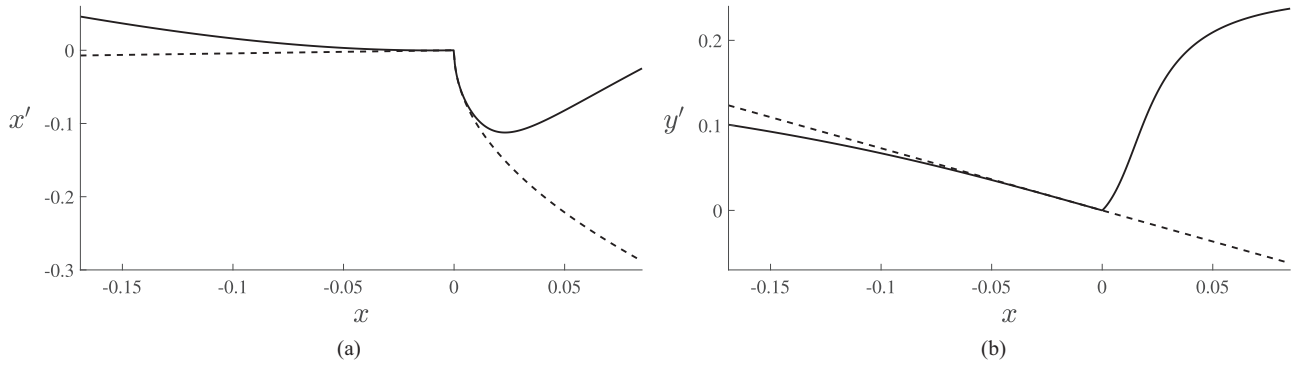


FIG. 10. Slices of Fig. 9 at $y = 0$ (dashed: Nordmark map; solid: Poincaré map).

certainly unrelated to the narrow-band chaos we wish to understand.

Figure 8(a) shows a bifurcation diagram of the system represented by the differential equations (12) in the coordinates of the Nordmark map. This was produced by applying the coordinate change to Fig. 4. Additional numerical continuation was employed to identify selected low-period solutions. Figure 8(b) shows a bifurcation diagram of the Nordmark map on the same scale. Clearly the chaotic attractor shown in Fig. 7 occurs at values of μ that are too large to be connected to the narrow-band chaos.

It is instructive to compare the two bifurcation diagrams of Fig. 8. For the impact oscillator (12) (left figure), the stable fixed point coexists with the chaotic attractor as the value of μ approaches 0 from below. An unstable period-2 solution is created at the grazing bifurcation and then becomes stable very shortly afterward (in a period-doubling bifurcation at $\mu \approx 0.000178$).

For the Nordmark map (right figure), the stable fixed point coexists with a stable period-3 solution. An unstable period-2 solution is created at the grazing bifurcation but does not become stable until a period-doubling bifurcation at $\mu \approx 0.1438$. In fact, the chaotic attractor in this case occurs close to this period-doubling bifurcation.

In both cases, the size of the basin of attraction of the fixed point appears to shrink to zero at the grazing bifurcation immediately beyond which there is no local attractor and so typical iterates of the map converge to a global object. This is characteristic of a dangerous border-collision bifurcation. Bifurcations responsible for the creation of the chaotic attractor in Fig. 8(a) were identified for similar parameter values in [11]. It was found that two *unstable* period-3 solutions are born at a grazing-induced saddle-node bifurcation, and when the period-1 solution becomes unstable at grazing, nearby orbits converge to the unstable manifold of one of the period-3 solutions, creating a chaotic attractor.

The global shapes of the Nordmark map, call it N , and Poincaré map P differ quite significantly. The upper panels of Fig. 9 show N evaluated at the grazing bifurcation; the lower panels show P in the coordinates of N and for the same parameter values. We observe that on the scale of the chaotic attractor (shown in the lower panels), P differs wildly from N in some places. In particular, P has a “hump” in the lower right corner while N does not. For this reason, it is not surprising that the global dynamics of P and N differs significantly, and

we feel that these differences explain why N does not exhibit a chaotic attractor at the grazing bifurcation.

The Nordmark map N does provide a reasonable approximation to P in a small neighborhood of the switching manifold. This is evident in Fig. 10, which shows N and P at a fixed value of y . By construction, N has the same \sqrt{x} -term as P in panel (a) and no \sqrt{x} -term like P in panel (b). However, N does not capture the higher-order x -term of $x > 0$, as can be seen in panel (b) (see [17] for a calculation of this term).

We also remark that in general Poincaré maps can be difficult to define globally. Generically there are points on the Poincaré section for which the return trajectory has a tangency to the Poincaré section resulting in a discontinuity in the Poincaré map [23]. To produce Fig. 9, this issue was circumvented by choosing subsequent intersections with the Poincaré section in a way that yields a continuous map.

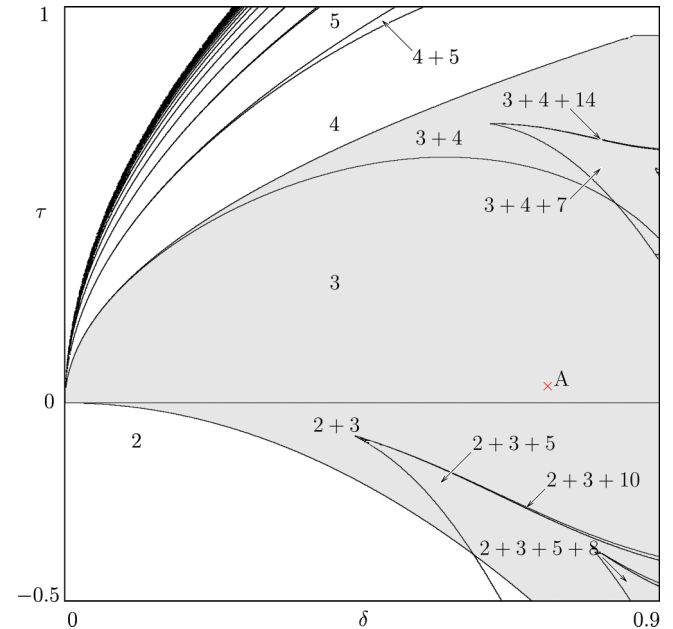


FIG. 11. A two-parameter bifurcation diagram of the Nordmark map (1) with $\chi = 1$. Regions are labeled by the period of stable periodic solutions that exist at $\mu = 0$ in addition to the fixed point undergoing grazing bifurcation. The period-3 region is shaded and we use plus signs to indicate where regions overlap. Parameter values corresponding to Fig. 7 are indicated by the point A.

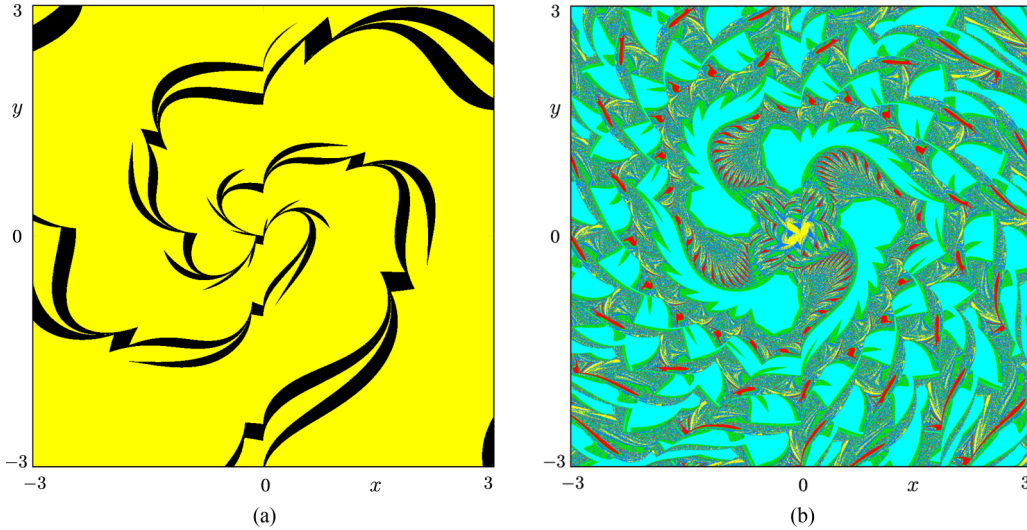


FIG. 12. Basins of attraction of the Nordmark map (1). In panel (a) $\tau = 0.0422$, $\delta = 0.7311$, $\chi = 1$, and $\mu = -0.07$ (before the grazing bifurcation shown in Fig. 7). The basin of the period-3 solution is yellow; the basin of the period-1 solution is black. In panel (b) $\tau = 0.5$, $\delta = 0.97$, $\chi = 1$, and $\mu = 0$. Shown are the basins of period-3 (yellow), period-4 (cyan), period-7 (blue), period-11 (green), and period-15 (red) solutions.

The stroboscopic map studied in [12] does not have this problem, so it is advantageous in this respect. In this paper, we have used a Poincaré map in order to produce a quantitative comparison to the Nordmark map.

VIII. COEXISTING STABLE SOLUTIONS IN THE NORDMARK MAP

While the Nordmark map does not exhibit narrow-band chaos, it does predict the excursion to large amplitude oscillations when the period-1 solution undergoes grazing.

Figure 11 shows a two-parameter bifurcation diagram of the Nordmark map with $\mu = 0$. It shows a period-incrementing structure issuing from the codimension-2 point $\delta = \tau = 0$ and formed by pairwise overlapping regions corresponding to periods 2, 3, 4, and so on. Parameter values corresponding to Fig. 7 belong to the period-3 region (shaded), as described above.

Basins of attraction for two examples are shown in Fig. 12. Panel (a) pertains to the parameters used in Fig. 7 at a value of $\mu < 0$ slightly before the grazing, and it shows the basin of attraction of the period-1 solution (black) and that of the period-3 solution (yellow). As $\mu \rightarrow 0$, the strips forming the basin of the period-1 solution become more narrow, vanishing at $\mu = 0$. For other values of the parameters, this phenomenon can involve a period- n solution, where n is not necessarily 3. Past $\mu = 0$, at which the basin of attraction of the period-1 solution vanishes, nearby orbits converge to the period- n solution.

Figure 12(b) shows basins of attraction for parameter values at which the Nordmark map with $\mu = 0$ has stable period- n solutions for $n = 3, 4, 7, 11$, and 15. The basins have a complex structure and are possibly “riddled” [24,25].

Since before the grazing bifurcation the basin of the period-1 solution is embedded in the basin of the period-3 solution (similar to the previous example), after the grazing bifurcation

nearby orbits are likely to converge to the period-3 solution instead of one of the stable higher period solutions. But certainly the presence of coexisting attractors with intermingled basins is a source of additional unpredictability in the system.

IX. CONCLUSIONS

We have shown that the Poincaré map P differs significantly from the Nordmark map N on the scale of the narrow-band chaotic attractor (Fig. 9). This manifests as a “hump” in the shape of P that may be attributed to return trajectories taking a substantially longer time to return to the Poincaré section than the period of the forcing [Fig. 3(b)]. While the dynamics of P may be quite complicated and fragile (in that many types of attractors exist over relatively small parameter regimes; see [12]), we believe that the shape of P is relatively robust because small changes to the parameters do not alter the qualitative properties of the vector field on a global scale (and we have observed this numerically).

We conclude that N does not exhibit narrow-band chaos because of its large deviations from P , and therefore the narrow-band chaos is a truly global phenomenon. The relatively large difference between N and P for small $x > 0$ shown in Fig. 10 is typical for maps with a series expansion that involves fractional powers because the error is of higher order than if only integer powers are involved [9].

Both N and P exhibit a stable period-1 solution before the grazing bifurcation but no local attractor immediately after the grazing bifurcation. Thus if the bifurcation parameter is slowly increased *dynamically*, we can expect the solution to jump from the period-1 solution to a coexisting large-amplitude attractor at the grazing bifurcation. As shown in Sec. VIII, it is possible that multiple large-amplitude attractors coexist, which adds significantly to the complexity of this phenomenon.

The quantitative comparison achieved here may prove useful for other types of grazing bifurcations and discontinuity-induced bifurcations more generally. Canonical forms (such as the border-collision normal form [26] and the Nordmark map N) adequately capture the dynamics in some neighborhood of the bifurcation, but little is known about the typical size of such a neighborhood. It also remains to be seen if a simple and geometrically meaningful term can be added to N to produce a better match to P , such as linear terms to account for higher-order terms in the discontinuity map [17].

ACKNOWLEDGMENTS

We thank the International Centre for Theoretical Sciences (ICTS), India, for enabling us to participate in the summer program on Dynamics of Complex Systems in 2018 (Code: ICTS/dcs2018/06), during which the idea of this paper was born. S.B. acknowledges financial support in the form of J.C. Bose Fellowship by the SERB, Govt. of India, No. SB/S2/JCB-023/2015. The work of V.A. was supported by the German Research Foundation Project No. AV 111/2-1.

-
- [1] R. Ibrahim, *Vibro-Impact Dynamics*, Lecture Notes in Applied and Computational Mechanics Vol. 43 (Springer, New York, 2009).
- [2] *Applied Nonlinear Dynamics and Chaos of Mechanical Systems with Discontinuities*, edited by M. Wiercigroch and B. de Kraker (World Scientific, Singapore, 2000).
- [3] J. de Weger, W. van de Water, and J. Molenaar, *Phys. Rev. E* **62**, 2030 (2000).
- [4] F. Peterka and J. Vacik, *J. Sound Vib.* **154**, 95 (1992).
- [5] A. Nordmark, *J. Sound Vib.* **145**, 279 (1991).
- [6] D. Li, H. Chen, J. Xie, and J. Zhang, *J. Phys. A* **50**, 385103 (2017).
- [7] P. Miao, D. Li, Y. Yue, J. Xie, and C. Grebogi, *Physica D* **398**, 164 (2019).
- [8] W. Chin, E. Ott, H. E. Nusse, and C. Grebogi, *Phys. Rev. E* **50**, 4427 (1994).
- [9] M. di Bernardo, C. Budd, A. Champneys, and P. Kowalczyk, *Piecewise-smooth Dynamical Systems. Theory and Applications* (Springer-Verlag, New York, 2008).
- [10] A. Nordmark, *Nonlinearity* **14**, 1517 (2001).
- [11] S. Banerjee, J. Ing, E. Pavlovskaja, M. Wiercigroch, and R. K. Reddy, *Phys. Rev. E* **79**, 037201 (2009).
- [12] E. Pavlovskaja, J. Ing, M. Wiercigroch, and S. Banerjee, *Int. J. Bifurcation Chaos* **20**, 3801 (2010).
- [13] Note that in this context, the term “narrow-band” has to be understood in parameter space, referring to the fact that chaotic attractors are observed in a narrow parameter region around the bifurcation point. The attractors are characterized by a broad-band of involved frequencies, so in the frequency domain the phenomenon we consider represents broad-band chaos.
- [14] M. A. Hassouneh, E. H. Abed, and H. E. Nusse, *Phys. Rev. Lett.* **92**, 070201 (2004).
- [15] A. Ganguli and S. Banerjee, *Phys. Rev. E* **71**, 057202 (2005).
- [16] J. Ing, E. Pavlovskaja, M. Wiercigroch, and S. Banerjee, *Philos. Trans. R. Soc. A* **366**, 679 (2008).
- [17] J. Molenaar, J. de Weger, and W. van de Water, *Nonlinearity* **14**, 301 (2001).
- [18] D. Simpson, J. Hogan, and R. Kuske, *SIAM J. Appl. Dyn. Sys.* **12**, 533 (2013).
- [19] J. Meiss, *Differential Dynamical Systems* (SIAM, Philadelphia, 2007).
- [20] H. Dankowicz and A. Nordmark, *J. Phys. D* **136**, 280 (2000).
- [21] M. Fredriksson and A. Nordmark, *Proc. R. Soc. A* **456**, 315 (2000).
- [22] V. Avrutin, Zh. T. Zhusubaliyev, A. Saha, S. Banerjee, L. Gardini, and I. Sushko, *Int. J. Bifurcation Chaos* **26**, 1630040 (2016).
- [23] C. Lee, P. Collins, B. Krauskopf, and H. Osinga, *SIAM J. Appl. Dyn. Syst.* **7**, 712 (2008).
- [24] J. Alexander, J. A. Yorke, Z. You, and I. Kan, *Int. J. Bifurcation Chaos* **2**, 795 (1992).
- [25] E. Ott, J. Alexander, I. Kan, J. C. Sommerer, and J. A. Yorke, *Physica D* **76**, 384 (1994).
- [26] D. Simpson, *SIAM Rev.* **58**, 177 (2016).